Gamal *et al. Biochar* (2025) 7:73
https://doi.org/10.1007/s42773-025-00459-x

Biochar

ORIGINAL RESEARCH Open Access

Effect of metal loading and Ce addition on biochar-supported Co catalysts for CO_2 methanation

Ahmed Gamal[1,4], Mengqi Tang[2], Mohamed M. Chehimi[2*], Ahmed M. Khalil[3], Kenneth I. Ozoemena[4], Aboubakr M. Abdullah[1*] and Khouloud Jlassi[1*]

Abstract

CO_2 hydrogenation to methane is an interesting topic that can result in CO_2 mitigation, providing a solution for global warming. Using a sustainable catalyst in that process will be considered as a plus point that makes the whole system (material + application) an eco-friendly process. Therefore, scientists have focused on the biochar-supported catalysts used in the CO_2 methanation. The use of cobalt (Co) catalysts supported on sugarcane bagasse biochar (SCBB) has not been investigated for the methanation of CO_2. Therefore, this work investigated the Co/SCBB systems in the CO_2 methanation with different Co loadings starting from 0.1 to 0.8 $mmol_{Co\text{-}salt}/g_{SCB}$. In addition, the effect of Ce was studied, proving that Ce addition improved the catalytic activity significantly, as the catalyst 0.5Co-0.25Ce/SCBB showed the foremost conversion of CO_2 (60% at 500 °C) and the best selectivity of methane (80% at 430 °C). This research lays the foundation for utilizing Ce to enhance the catalytic properties of various transition metals that can not offer high catalytic activity alone in the carbon dioxide methanation.

Highlights

- Sustainable catalysts for CO_2 hydrogenation to methane help mitigate CO_2 emissions and combat global warming.
- Co supported on sugarcane bagasse biochar (SCBB) for CO_2 methanation is a novel approach not previously reported.
- Adding cerium (Ce) to the Co/SCBB catalyst significantly improved CO_2 conversion and methane selectivity.

Keywords Cobalt-based catalysts, Hydrogenation, Methanation, Biochar, Methane, CO_2

*Correspondence:
Mohamed M. Chehimi
mohamed.chehimi@ycnrs.fr
Aboubakr M. Abdullah
bakr@qu.edu.qa
Khouloud Jlassi
khouloud.jlassi@qu.edu.qa
Full list of author information is available at the end of the article

Springer

© The Author(s) 2025. **Open Access** This article is licensed under a Creative Commons Attribution 4.0 International License, which permits use, sharing, adaptation, distribution and reproduction in any medium or format, as long as you give appropriate credit to the original author(s) and the source, provide a link to the Creative Commons licence, and indicate if changes were made. The images or other third party material in this article are included in the article's Creative Commons licence, unless indicated otherwise in a credit line to the material. If material is not included in the article's Creative Commons licence and your intended use is not permitted by statutory regulation or exceeds the permitted use, you will need to obtain permission directly from the copyright holder. To view a copy of this licence, visit http://creativecommons.org/licenses/by/4.0/.

Graphical Abstract

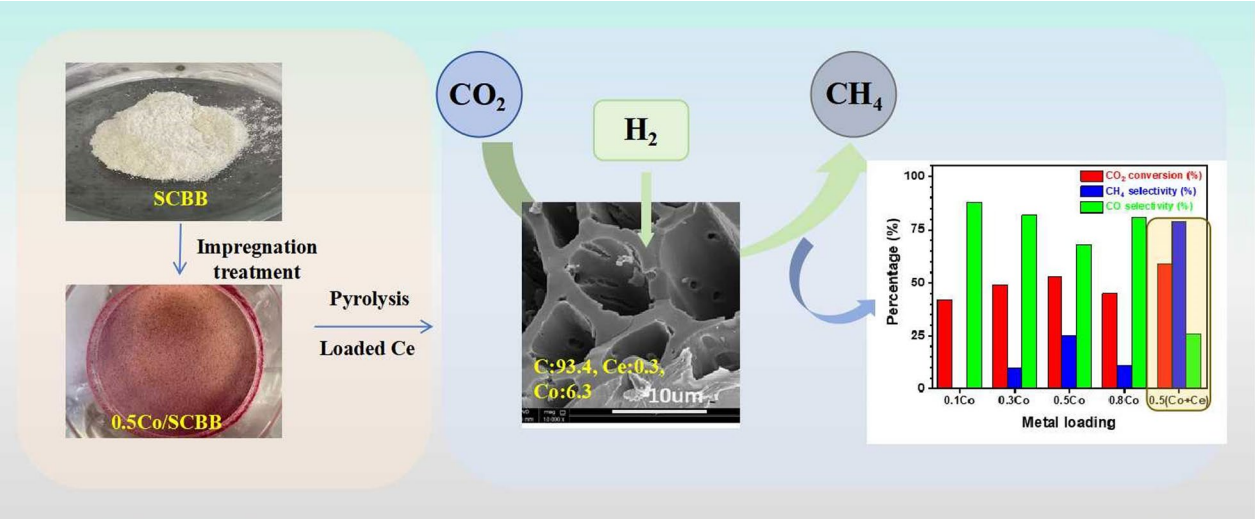

1 Introduction

In recent times, there has been considerable focus on the issue of global warming caused by the buildup of green-house gases in the atmosphere, particularly carbon dioxide, leading to the deterioration of the whole environment. Based on present estimates, to have a 2 in 3 chance of limiting the global temperature increase to less than 2 °C by 2100, carbon dioxide emissions must be cut down to less than 5 billion tons annually before 2050 (Valluri et al. 2022). To put this in perspective, the amount of current emissions is about 48 billion tons of CO_2 per year (Valluri et al. 2022). Thus, carbon dioxide capture and utilization are crucial processes to mitigate the impact of CO_2. However, transformation of CO_2 into chemicals and/or energy products such as methane through the CO_2 methanation path is more promising, as it not only decreases the emissions of CO_2, but also provides additional economic value (Gamal et al. 2024).

Methane is progressively asserting itself as the primary energy source in comparison to coal. The notion of obtaining it from renewable carbon sources instead of extracting natural gas holds even greater appeal. Biomass-derived methane presents itself as a compelling prospect for effective power generation, providing the benefit of an almost closed CO_2 cycle (Collet et al. 2017). In addition, hydrogenation of CO_2 to methane (methanation) is a perfect way to mitigate the CO_2 in the environment as well as providing a valuable product (methane), which can be represented by Eq. 1. However, manipulating the reaction temperature and the stoichiometric ratios can lead to redirecting the reaction to produce carbon monoxide instead of methane, as depicted in Eq. 2, which then reacts with the produced water to produce methanol (Tripodi et al. 2020; Song et al. 2023).

$$CO_2 + 4H_2 \Rightarrow CH_4 + 2H_2O \; \Delta H = -165 \text{kJ/mol} \quad (1)$$

$$CO_2 + H_2 \Rightarrow CO + H_2O \; \Delta H = 41 \text{kJ/mol} \quad (2)$$

Transition and noble metals are intensively reported for CO_2 methanation, particularly ruthenium (Shen et al. 2024), nickel (Zhong 2024), and cobalt (Zhong et al. 2023) supported on various materials, such as silica and alumina (Riani et al. 2023). However, the low cost of the Earth abundant transition metals makes them more favored than the noble metals and their high cost and scarcity preclude their use (Zhang 2022; Gac et al. 2020; Frontera et al. 2017). Pyrolysis of biomass, conducted in the slow regime (Pawelczyk et al. 2022), results in high portion of biochar, which is the solid product usually exhibiting high surface area (Leng et al. 2021; Wiśniewska et al. 2022).

Several agrowastes can be pyrolyzed into biochar, such as date and olive pits, fruit peels, rose petals, forestry waste, marine algae, and sugarcane bagasse, to name but a few (Khalil et al. 2021; Bhakta 2023; Adeniyi et al. 2023). However, biochar is rarely reported as a support material for the CO_2 methanation reactions, particularly, the biochar of the sugarcane bagasse. The latter offers porous and high surface area structures (Snoussi et al. 2023), which can enhance the metal dispersion, leading to better catalytic performance (Zhu et al. 2016). Particularly, the

wet impregnation technique allows to obtain sugarcane bagasse biochar (SCBB) loaded with evenly dispersed metallic and bimetallic, as well as metal oxide nanocatalysts for water treatment (Tang et al. 2023; Tang et al. 2024). Taking advantage of this unique behavior of SCBB (not noted for example with previous work on olive pit biochar), we reasoned that slow pyrolysis applied to the wet impregnation process would be a valuable approach to directly obtaining Co nanocatalysts immobilized on SCBB, a support that has never served for the immobilization of Co. This is what has motivated the development of Co-decorated biochar for the thermo-catalytic reactions of CO_2 methanation.

Hence, sugarcane bagasse biochar was prepared as a support for Co, investigating its catalytic performance in the methanation reactions. Furthermore, the impact of Co loadings was explored via synthesizing and testing catalysts with various Co amounts (0.1–0.8 $mmol_{Co\text{-}salt}/g_{SCB}$). In addition, the effect of Ce addition on the catalytic performance was also investigated, which showed an interesting impact, improving the catalytic activity. This work will open the door for using the SCBB as a sustainable support in various reactions extending beyond just CO_2 methanation.

2 Methodology

2.1 CO_2 methanation

The reactions were run in a tubular flow reactor, as seen in Fig. 1. All tests were performed at a wide range of temperatures (200–500 ℃), and 1 atm. A total of 0.5 g of the catalyst was loaded between two pieces of quartz wool, and a 40 sccm of 40% H_2 and 10%CO_2 in argon (WHSV = 48000 ml g^{-1} h^{-1}) was introduced to the reactor. It is important to note that the biochar is a fluffy material that offers sufficient contact between the gas and the catalyst. The effluent gases passed through a condenser unit, where water was removed, and then the gases were pushed to an IR analyzer (Yokojawa-IR200) for analysis. The IR bands corresponding to the gas-in and gas-out confirmed that the change occurred in the gases and the carbon dioxide methanation reaction could be monitored with the described setup.

In the beginning, all samples were pretreated by 10 vol.% of H_2/Ar for one hour at 500 °C. Then, the temperature of furnace was decreased to 25 °C, and the gases were passed to the tested sample as the temperature was increased to 500 °C. The following definitions were used in our calculation of carbon dioxide conversion (Eq. 3), selectivity of methane (Eq. 4) and also methane yield (Eq. 5)and reaction rates (Eq. 6) (Ali et al. 2020; Ali et al. 2023).

$$\%CO_2 = [n(CO_{2\,In} - nCO_{2\,Out})/nCO_{2\,In}] \times 100 \quad (3)$$

$$\%CH_4 = [nCH_{4\,Out}/[nCO_{2\,In} - nCO_{2\,Out}] \times 100 \quad (4)$$

$$\%CH_4 = [nCH_{4\,Out}/nCO_{2\,In}] \times 100 \quad (5)$$

$$r = (nCO_2In - nCO_2Out)/g_{cat}.\,T_{min} \quad (6)$$

2.2 Synthesis

The gathered leftover fibrous waste specimens (SCB) were broken down using a powered household grinding device, followed by additional pulverizing using a device for crushing coffee beans. The resulting fine material was then filtered through a mesh, and employed as an organic raw material for the synthesis of biochar-based catalysts. Co nitrate hexahydrate ($Co(NO_3)_2{\cdot}6H_2O$) was utilized as a precursor for the wet impregnating process of

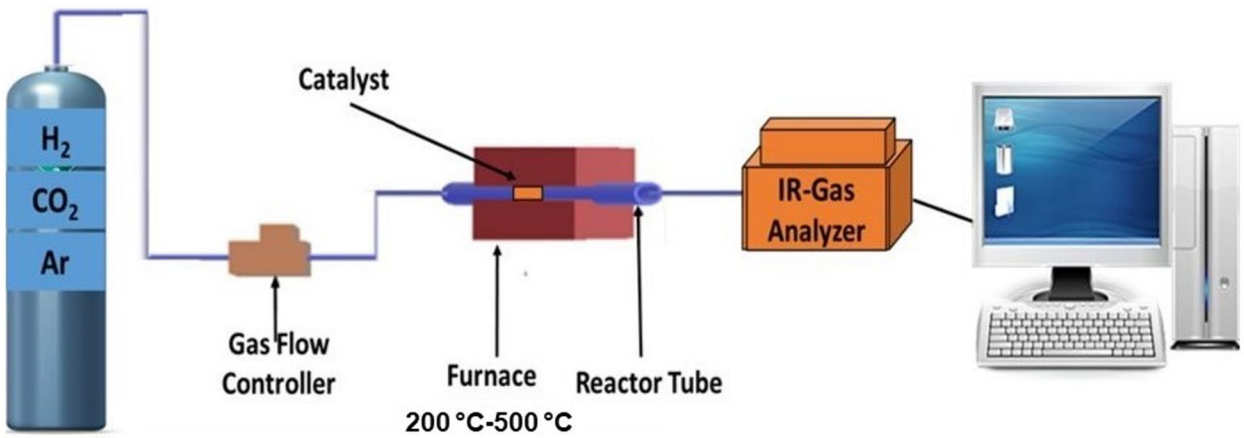

Fig. 1 A scheme illustrating the experimental apparatus

Co into the biochar. 87.31, 261.93, 436.55, and 698.48 mg of $Co(NO_3)_2{\cdot}6H_2O$ were dissolved in five different beakers containing 20 mL of deionized water including the prepared sugarcane bagasse powder, representing the molar mass ratio of 0.1, 0.3, 0.5, and 0.8 Co nitrates hexahydrate per gram of sugarcane bagasse (mmol g^{-1}), respectively, as shown in Table 1. The solutions (xCo/SCB) were dried at 80 °C, and then the dried mixture was transferred into a tubular furnace and pyrolyzed at 500 °C in nitrogen atmosphere for one hour, with a heating rate of 10 °C min^{-1}, and then cooled down to the room temperature.

The yield of the collected samples varied from 23 to 28 weight percent, as seen in Table 1. The as-synthesized catalysts were labeled as 0.1 Co/SCBB, 0.3 Co/SCBB, 0.5 Co/SCBB and 0.8 Co/SCBB, according to the aforementioned molar mass ratios ($mmol_{Co\text{-}salt}/g_{SCB}$). In addition, impregnation, mechanical mixing, and then thermal reduction were used to prepare the bimetallic catalyst Co-Ce/SCBB. 72.76 mg of $Co(NO_3)_2{\cdot}6H_2O$ was dissolved in 20 mL of deionized water including 1 g of the pure SCBB, representing the molar mass ratio of 0.25 mmol g^{-1}_{SCBB}, followed by the same aforementioned procedures of drying and calcination. Then, 108.56 mg of $Ce(NO_3)_3{\cdot}6H_2O$, representing similar molar mass ratio of 0.25 mmol g^{-1}_{SCBB}, was mechanically mixed with the 0.5 Co/SCBB, followed by thermal reduction by hydrogen at 500 °C for one hour, with a heating rate of 10 °C min^{-1}. The collected catalyst after reduction was labeled as 0.5 Co-0.25 Ce/SCBB with a total metal loading of 0.5 mmol g^{-1} to be compared with the catalyst 0.5 Co/SCBB that presented the highest catalytic performance among the monometallic catalysts. Furthermore, metal-free and Ce/SCBB samples were prepared and tested for the same process and both of them were inactive and could not catalyze the CO_2 methanation reaction.

2.3 Characterization

Nova Nano SEM machine was utilized to obtain images of the synthesized catalysts. Transmission Electron Microscopy (TEM) was employed for topographical and morphological images using FEI-TECNAI-G2-TEM and TF20. XRD-PANalytical-EMPYREAN was employed to characterize the structure of the catalysts. XPS surface chemical analysis was performed using a K Alpha + machine (Thermo, UK) for the pristine and impregnated samples. The machine is fitted with a monochromated Al Kα source (1486.6 eV) and a flood gun to compensate for the static charge build-up. Raman spectra were acquired using a Horiba HR 800 instrument fitted with He–Ne laser beam set to 633 nm. The signals were recorded in the 800–2700 cm^{-1} spectral region. A Pyris-6 TGA-PerkinElmer (Waltham MA, USA) was employed for thermal gravimetric analysis (TGA) in air. The heating rate was 10 °C min^{-1}, and the thermograms were recorded in the range of 25 to 800 °C.

3 Results and discussion

3.1 Characterization of the catalytic biochar materials

The SEM analyses of all catalysts exhibited honeycomb-like structures including almost hexagonal arrays of pores of the bimetallic catalyst 0.5 Co-0.25 Ce/SCBB (Fig. 2a–c). Those structures can provide a high porous surface area, which enhances active site revelation, leading to elevated catalytic performance (Zhu et al. 2016). Furthermore, Fig. 2d, e displays the fishing net structures of the 0.5 Co-0.25 Ce/SCBB found in all samples, which matches the previously reported results (Gamal et al. 2024). The pores of fishing nets were elongated like slits with an average length of 2–5 µm and around 1 µm width as seen in the yellow circled area of Fig. 2e. The formation of those uniformed pores, which are ordered in a fishing net structure, is attributed to the dehydration of the cell structure of the sugarcane bagasse (Tang 2023). The EDX analysis of samples indicated the metal loadings of Co into the sugarcane bagasse biochar. The EDX analysis of the bimetallic 0.5 Co-0.25 Ce/SCBB confirmed the existence of Co and cerium in the catalyst with roughly atomic percentages of 7.12 and 4.52, respectively, and approximately weight percentage of 10 for each, as seen in Fig. 2f.

The TEM images of the monometallic catalyst 0.5 Co/SCBB showed that the Co nanoparticles were not well distributed on the support, as some agglomerations were

Table 1 The parameters used for synthesis

Catalyst	Sugar cane bagasse (g)	Co-Nitrates (mg)/(mmol.)	H_2O (mL)	Biochar Mass (g)/Yield (%)	Parameter
SCBB	5.013	/	/	1.338/26.69	Temp.: 500 °C Heating rate: 10 °C/min Residence time: 1 h Gas: N_2
0.1 Co/SCBB	3.000	87.31/0.1	20	0.715/23.17	
0.3 Co/SCBB	3.000	261.93/0.3	20	0.843/25.87	
0.5 Co/SCBB	3.000	436.55/0.5	20	0.942/27. 46	
0.8 Co/SCBB	3.000	698.48/0.8	20	1.0552/28.63	

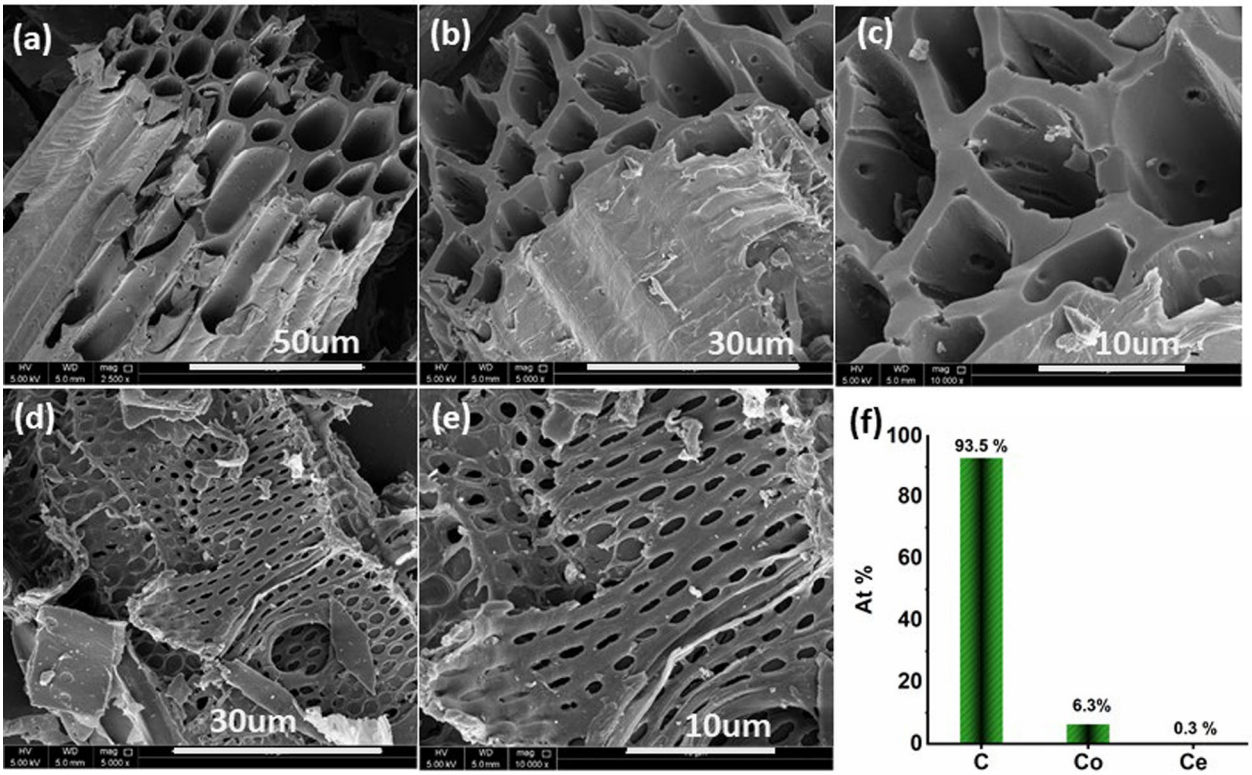

Fig. 2 SEM images of the bimetallic catalyst 0.5 Co-0.25 Ce/SCBB at different magnifications, showing the pore structure (**a–c**) and the fishing net structures (**d, e**). **f** EDX analysis of the tbimetallic catalyst 0.5 Co-0.25 Ce/SCBB

always found in different spots of the catalyst, as seen in Fig. 3a–c. In addition, the particle size of the monometallic catalyst 0.5 Co/SCBB was not uniform and showed a wide range of particle sizes starting from 10 to 35 nm, calculated by ImageJ software. However, the rough mean size of the nanoparticles of the monometallic 0.5 Co/SCBB was 18.5 nm, as shown in the inserted histogram of Fig. 3c. On the other hand, the bimetallic catalyst 0.5 Co-0.25 Ce/SCBB exhibited good metal distribution on the support, as seen in Fig. 3d–f, which was attributed to the effect of Ce that improved the metal dispersion on the support (Hu et al. 2019; Renda et al. 2021), resulting in higher catalytic performance. Moreover, 0.5 Co-0.25 Ce/SCBB presented uniformed nanoparticles with an average size of 11.5 nm, which is smaller than that of the monometallic 0.5 Co/SCBB (18.5 nm), as shown in the inserted histogram of Fig. 3e. Moreover, the TEM images indicated that Co and Ce were more like distributed on the surface of the biochar, providing more metal exposure.

XPS analysis was performed to monitor the surface modification of the biochar as a result of Co nitrate loading, and also the addition of cerium to 0.5 Co/SCBB hybrid.

The elemental surface composition is reported in Table SI1. Figure 4 displays XPS analyses, *i.e.* the survey regions (Fig. 4a) and the Co/(C + N) and (Co + Ce)/(C + N) atomic ratios versus the intial loading of Co nitrate (Fig. 4b), deduced from the data reported in Table SI1. Figure 4a shows neat spectrum of pure SCBB biochar exhibiting a sharp C1 s peak at 285 eV and O1 s at 532 eV. There was an additional Co2p doublet for 0.5 Co/SCBB sample. The inset shows $Co2p_{3/2}$ centered at 780.4 eV due to surface oxidation of Co (Cho et al. 2018), shadowing the shoulder at 778.5 eV assigned to zero-valence Co (Powell 2012). After pyrolysis of the cerium nitrate and 0.5 Co/SCBB mixture, Ce3 d is hardly noticed on the survey spectrum, and Ce3 d is clearly visible only after scanning the Ce3 d narrow region. This complex region shows a first series of 3 peaks centred at 882.7, 888.8 and 898.7 eV assigned to Ce3 $d_{5/2}$, and a second series of 3 peaks centred at 901.2, 906.9 and 916.9 eV, assigned to Ce3 $d_{3/2}$ (Bhuvanendran et al. 2021; Jiao et al. 2021). The very last peak exists

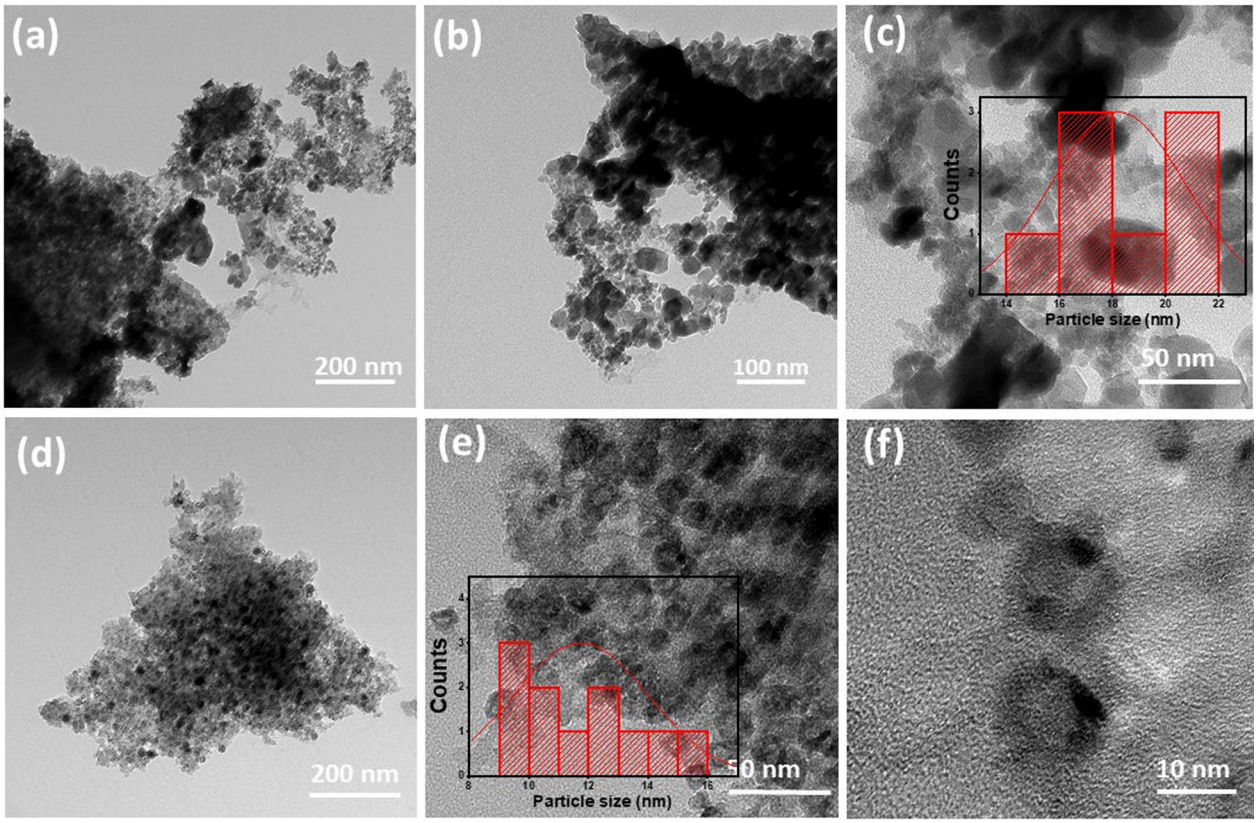

Fig. 3 TEM images of o.5 Co/SCBB (**a–c**) and 0.5 Co-0.25 Ce/SCBB (**d–f**). Insets of **c** and **d** show nanoparticle size distribution

for cerium (IV) oxidation only.[1] Despite the noisy signal of Ce3 d, the two first peaks at 882.7 and 888.8 eV are not well resolved, possibly due to the contribution of a minor Ce3 $d_{5/2}$ peak at 885.9 eV, from Ce(III) (Jiao et al. 2021; Praline et al. 1980). Therefore, the Ce3 d regions is mostly due to CeO_2 (Bhuvanendran et al. 2021), but without excluding Ce(III).

Figure 4b shows a graph of the Co(C +N) atomic ratio against the original mass loading of the Co nitrate on the biomass. A stepwise increase of this atomic ratio indicated excellent control over the preparation and the surface composition of the biochar samples. After 0.8 mmol g^{-1} biomass loading, saturation started to be noted. Above 0.8 mmol g^{-1} biomass, the Co nitrate was likely to yield agglomerated Co nanoparticles on the biochar with quasi-no CO_2 methanation activity. For the 0.5 Co-0.25 Ce/SCBB, the ratio seemed slightly higher than that of the original sample 0.5 Co/SCBB and this could be ascribed to the grinding of this biochar with cerium nitrate. The (Co +Ce)/(C +N) was slightly higher than the reference values for this biochar, which is in line with the contribution of cerium.

To account for oxygen vacancy, the main high-resolution O1 s peaks were fitted for SCBB (Fig. 4c), 0.5 Co/SCBB (Fig. 4d), and 0.5–0.25 Ce/SCBB (Fig. 4e), respectively. There is possibly a small portion of mineral oxides in SCBB (trace amounts of K_2O and NaO resulting from the pyrolysis process). The main peak is due to the underlying biochar and is assigned to C= O and C–OH species. Wet impregnation induces the addition of CoO as Co is partially oxidized (see inset of Fig. 4a). The peak is at 530.0 eV, in line with the average value 529.9 ±0.35 eV (CoO) calculated using the values indexed in the NIST XPS Database. The peak at 533–533.3 eV is due to C–O–C from the biochar. The main component could now have a contribution of oxygen vacancies, reported usually in the 531–532 eV binding energy range. However, this assignement is controversial (Wang et al. 2024) and confirmation should be provided by more research groups. Figure 4e shows a complete change in the shape of the O1 s narrow region; a contribution of CeO_2 is now implemented at 529.3 eV which accounts for the average value 529.2 ±0.3 eV calculated using the NIST XPS

[1] See https://www.thermofisher.com/fr/fr/home/materials-science/learning-center/periodic-table/lanthanide-rare-earth/cerium.html, last accessed 12 December 2024.

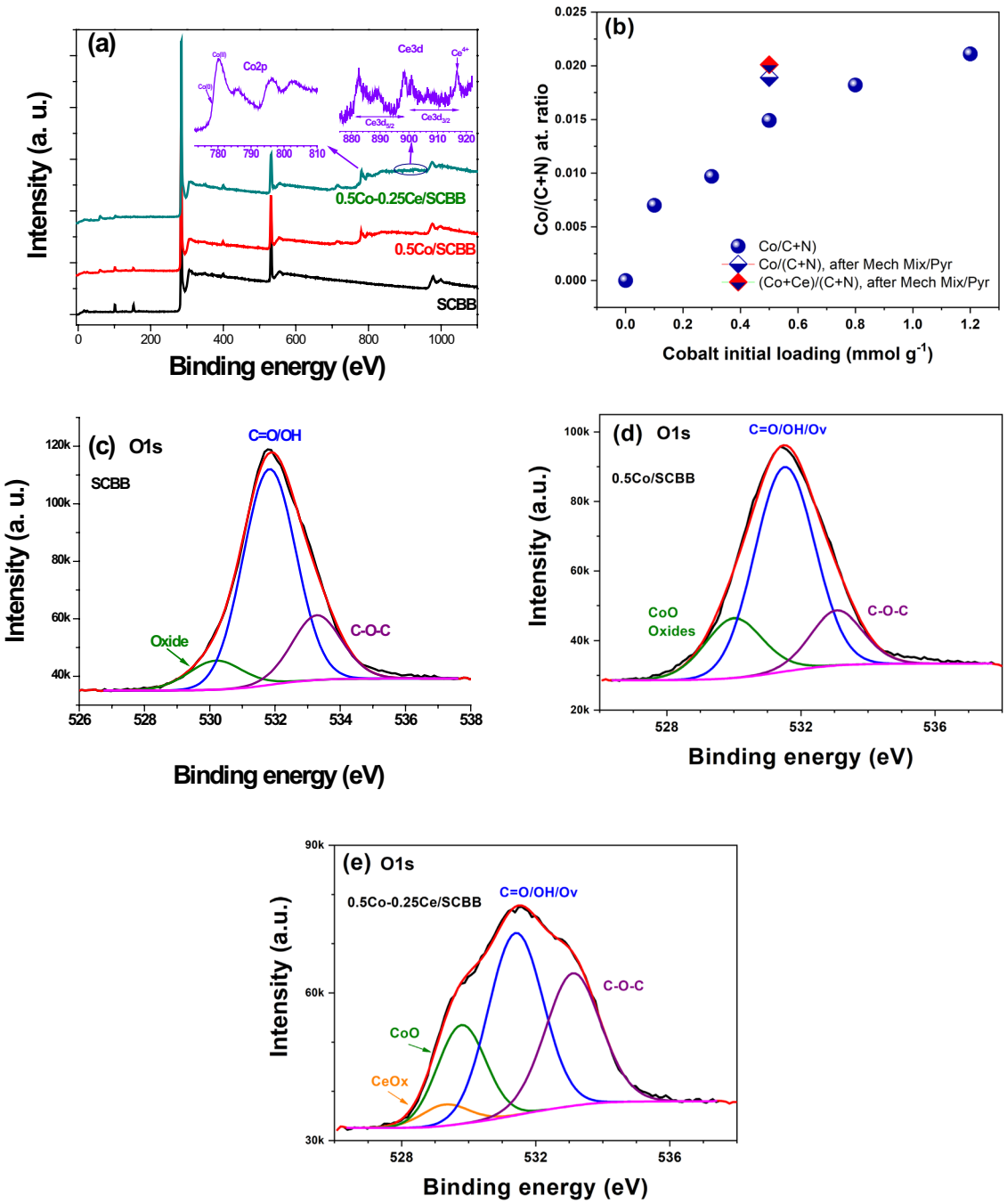

Fig. 4 XPS analysis of biochar samples: **a** survey spectra of SCBB, 0.5 Co/SCBB before, and after CeO_2 addition, **b** Co/(C + N) atomic ratio versus the initial Co nitrate loading on the biomass. (Co + Ce)/(C + N) atomic ratio is also displayed for the cerium-containing sample. Peak-fitted O1 s spectra are shown for SCBB (**c**), 0.5 Co/SCBB (**d**), and 0.5 Co-0.25 Ce/SCBB (**e**)

Database. The main peak is assigned again to C = O/OH and possibly to oxygen vacancies. There is a dramatic increase in the proportion of C–O–C peak at 533.1 eV, possibly due to the oxidation of the 0.5 Co/SCBB upon mechanical mixing with cerium salt, thus resulting in mechanochemical oxidation of biochar carbon atoms. Although O1 s could be exploited to deduce the contribution of oxygen vacancies, it remains difficult to be accurately calculated given the contribution of biochar to O1 s in the 531–532 eV range.

The XRD analyses of all samples showed the successful impregnation of Co into the biochar support, as seen in Fig. 5a. All catalysts showed the broad peak of carbon located aroun 24.5 degree, which indicates the existence of the amorphous carbon (Yuan et al. 2013). The 0.1 Co/SCBB did not present peaks corresponding to the presence of Co, which was attributed to the low Co concentrations loaded into the biochar. However, 0.3 Co/SCBB, 0.5 Co/SCBB, and 0.8 Co/SCBB showed peaks around 42, 52, and 74, corresponding to the Co [111], [200], and [220] planes, respectively (Yuan et al. 2013). That indicates that Co mainly exists in the metallic phase with face-centered cubic structure (Yuan et al. 2013). In addition, increasing metal loading in catalysts resulted in sharper peaks with a little higher 2θ degrees, which may indicate increasing of crystalinity with increasing the metal amount.

The XRD analysis of the bimetallic catalyst 0.5 Co-0.25 Ce/SCBB did not show any clear peaks, which might be ascribed to the low concentrations of the both impregnated metals in the biochar. The Raman spectra analyses of the prepared catalysts showed a D band around 1344 cm^{-1} in addition to a G band about 1575 cm^{-1}, which approves the presence of amorphous and graphitic carbon, as seen in Fig. 5b. In addition, the Raman spectra confirmed the graphitization of the prepared samples as the peak intensity of the G band (IG) was always higher than the peak intensity of the D band (ID) in all synthesized samples. The ratio of ID/IG of the metal-loaded catalysts was around 0.8, which was

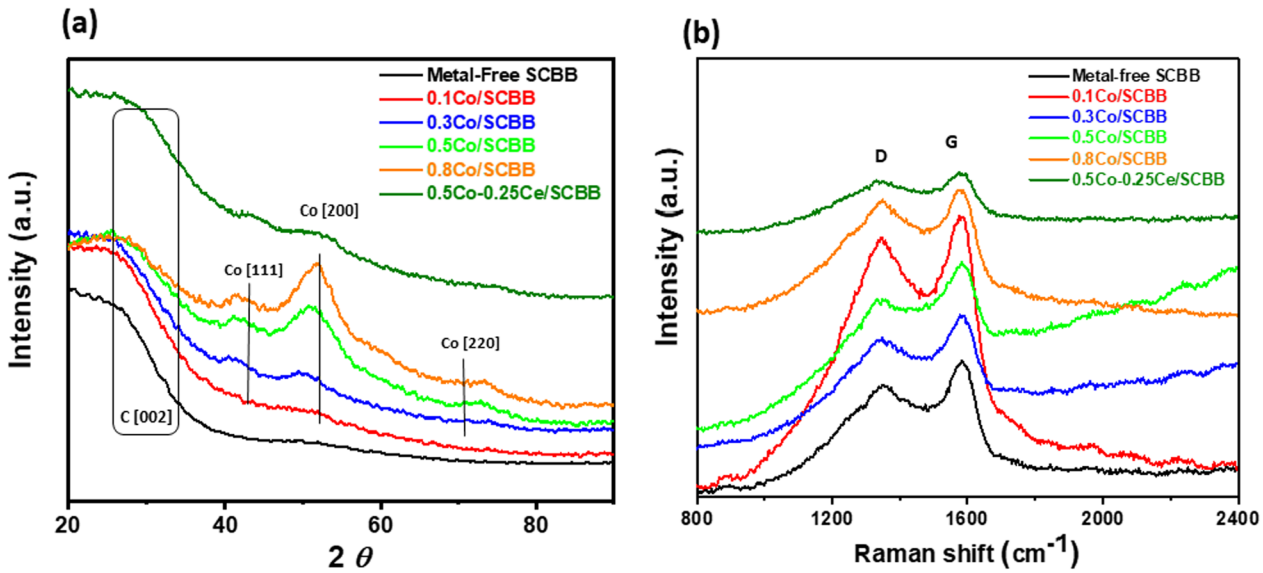

Fig. 5 **a** XRD diffraction patterns, and **b** Raman spectra of the prepared biochar-supported catalysts

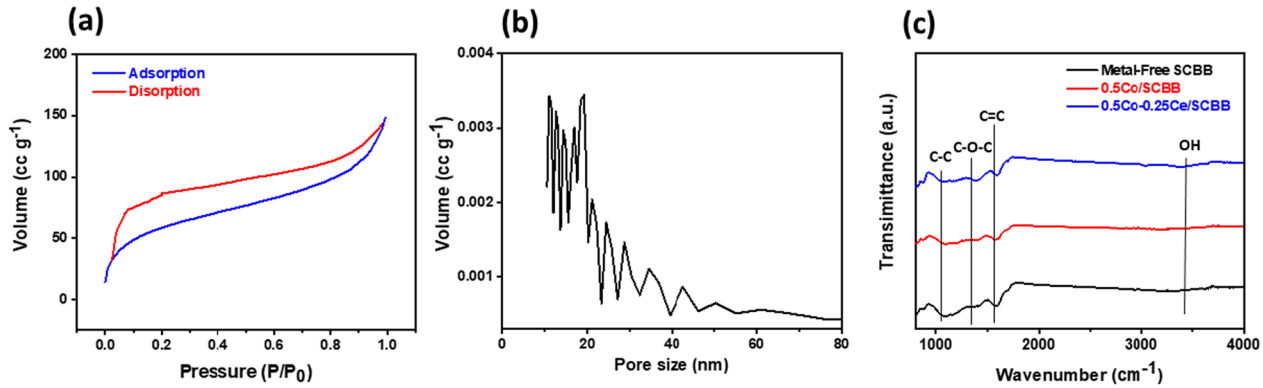

Fig. 6 The N_2-adsorption–desorption isotherm (**a**) and the HBH pore size distribution (**b**) of 0.5 Co-0.25 Ce/SCBB. **c** FTIR analysis of metal-free SCBB, 0.5 Co/SCBB, and 0.5 Co-0.25 Ce/SCBB

less than that of the pure SCBB (0.9), indicating that the addition of Co increased the graphitization of the catalysts.

Figure 6a shows the BET analysis of the bimetallic catalyst 0.5 Co-0.25 Ce/SCBB, which is similar in shape to the other prepared catalysts. All samples showed similar nitrogen adsorption–desorption isotherms, which are classified as type II isotherms, resulting from unrestricted monolayer-multilayer adsorption up to high p/p0, according to the IUPAC classification (Eddaoudi and (ACS Publications) 2005; Thommes et al. 2015). The hysteresis loops were also similar in shape, indicating the H4 type of the porous materials that include micro and meso pores (Thommes et al. 2015), as confirmed by the BJH pore size distribution, as depicted in Fig. 6b. The BET calculations exhibited that all catalysts owned high surface area, ascribed to the natural structures of the SCBB. The pattern of enhancing the specific surface area aligned with raising metal amounts, as shown in Table 2, which matches with previously reported results (Gamal et al. 2024), attributed to the ability of metals to carve away the exterior layer forming larger channels or holes, as demonstrated by the pore volume measurements (Gamal et al. 2024).

Accordingly, the blank support (SCBB without metal) presented the smallest specific surface area while the metal-loaded catalysts presented the highest surface area as shown in Table 2. In addition, the blank support showed the least pore volume while metal-loaded ones showed higher pore volume as shown in Table 2. The 0.5 Co/SCBB and 0.8 Co/SCBB had the same BJH value, which might occur because the catalyst was saturated with the amount of metal that is more than enough to carve away the exterior layer forming larger channels or holes.

Fourier-transform infrared spectroscopy (FTIR) analyses of all samples did not show clear changes in the position of peaks between the metal-free SCBB and the metal-loaded ones. However, it is worth noting that the peaks belonging to the metal-loaded catalysts were slightly broader, as shown in the FTIR spectra of 0.5 Co-0.25 Ce/SCBB and 0.5 Co/SCBB (Fig. 6c). Moreover, a small broad peak was observed at ~ 1200 cm^{-1}, which is attributed to the existence of C–O–C bonds (Chen et al. 2019). In addition, other peaks were noted around 1500 and 1700 cm^{-1}, ascribed to C–C and C = C bonds (Chen et al. 2019), respectively (Fig. 5c). The spectral broad bands, hardly appearing between 3175 to 3490 cm^{-1}, are attributed to the O–H stretching intramolecular hydrogen bonds (see Fig. 6c) (Kumar et al. 2014).

Table 2 BET and BJH calculations

Catalyst	BET SA $m^2 g^{-1}$	BJH PV cc g^{-1}
SCBB	162	0.08
0.1 C/SCBB	197	0.15
0.3 Co/SCBB	215	0.17
0.5 Co/SCBB	211	0.18
0.8 Co/SCBB	216	0.18
0.5 Co-0.25 Ce/SCBB	217	0.18

3.2 Catalytic performance

All samples were evaluated in the aforementioned system after activation in H_2 for 1 h at 500 °C. Figure 7a

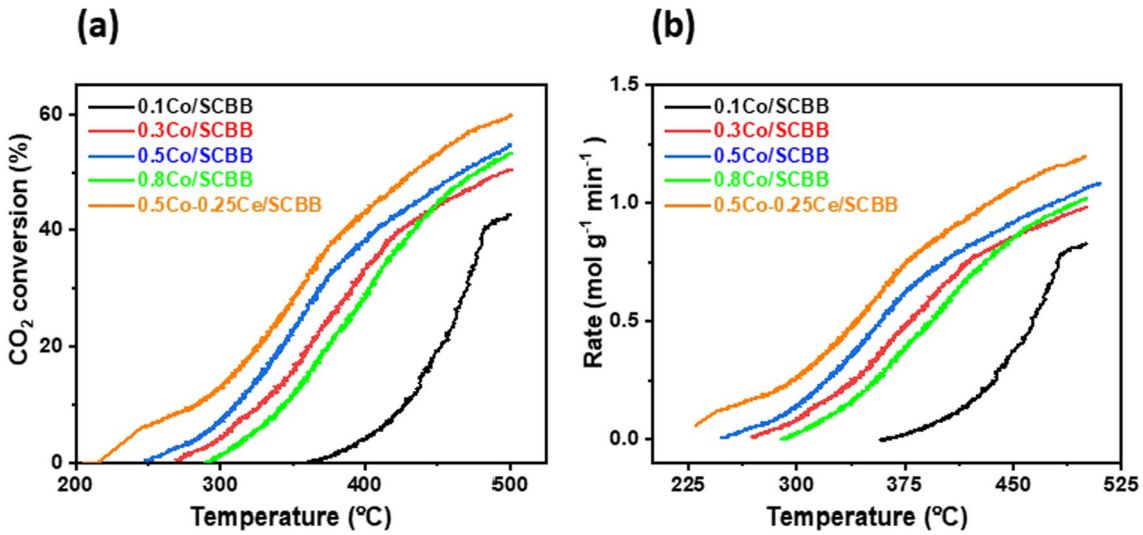

Fig. 7 CO_2 Conversion (**a**) and reaction rates (**b**) of all catalysts

exhibits the carbon dioxide conversion as a function of temperature from 200 to 500 °C. The blank samples that do not contain any loaded metals did not show any catalytic activity. However, all metal-loaded samples showed CO_2 conversion with different percentage, and 0.5 Co/SCBB showed the highest CO_2 conversion among the monometallic catalysts. However, the bimetallic catalyst 0.5 Co-0.25 Ce/SCBB was the most active one, showing 60% CO_2 conversion at 500 °C, attributed to the Ce effect, which enhanced the metal dispersion on the support. Furthermore, the reaction rates at different reaction temperatures were calculated to provide more understanding as seen in Fig. 7b. The reaction rate was increasing with increasing the temperatures and also with increasing the Co loadings, as the 0.5 Co/SCBB presented the best reaction rate amid the monometallic catalysts. 0.8 Co/SCBB displayed inferior activity than 0.5 Co/SCBB, attributed to the agglomeration brought about by the excess amounts of the impregnated Co. Moreover, the bimetallic catalyst Co-Ce/SCBB exhibited the highest reaction rate among all tested catalysts, attributed to the presence of Ce.

Figure 8a displays the selectivity of methane of all catalysts; all catalysts activated the methane production except 0.1 Ni/SCBB, which was ascribed to the small impregnated amount of Co. 0.5 Co/SCBB provided the highest methane production among the monometallic catalysts. However, the methane selectivity of all monometallic Co catalysts was low, as shown in Fig. 8a. Moreover, the bimetallic 0.5 Co-0.25 Ce/SCBB enhanced the methane selectivity interestingly. The methane selectivity of 0.5 Co/SCBB was ~25% at 430 °C, while 0.5 Co-0.25 Ce/SCBB presented ~80% methane selectivity at the same temperature. Increasing the temperature more than 430 °C led to less methane selectivity and higher carbon monoxide selectivity, attributed to the competitor RWGS (reverse water gas shift reaction) that is preferred to occur at the higher temperatures (Lee et al. 2021; Stangeland et al. 2020), which redirects the reaction to generate carbon monoxide rather than methane.

Figure 8b illustrates that the selectivity of CO was higher than methane selectivity for all monometallic catalysts at all reaction temperatures, indicating that Co alone is not really selective for methane production. However, addition of Ce decreased the selectivity of CO clearly, and the bimetallic 0.5 Co-0.25 Ce/SCBB showed only ~25% CO selectivity at 430 °C, which is the optimal temperature for CO_2 methanation. Figure 8c shows the methane yields, which were always low for all monometallic catalysts throughout the entire temperature range of this study. Addition of Ce increased the methane yield intensively, as the bimetallic 0.5 Co-0.25 Ce/SCBB achieved ~40% methane yield at 430 °C, and then decreased with increasing the reaction temperature, due to the reverse water gas shift reaction.

Figure 9a compares the catalytic activity of the catalysts at 430 °C, as an optimal condition for the reaction to be most selective to methane. The comparison displayed that the bimetallic catalyst 0.5 Co-0.25 Ce/SCBB offered the best CO_2 conversion, the highest methane production, and the lowest CO selectivity at the reaction temperature of 430 °C. This excellence performance is ascribed to the well metal nanoparticles distribution on the support and the small size of the nanoparticles offered by Ce. Since the bimetallic catalyst 0.5 Co-0.25 Ce/SCBB displayed the greatest activity, it was further evaluated for its stability towards CO_2 conversion, CH_4 selectivity, and CO selectivity at 430 °C for 12 h. As shown in Fig. 9b, the catalyst 0.5 Co-0.25 Ce/SCBB showed a stable performance without any deactivation during the whole reaction time, as the CO_2 conversion fluctuated around 51%, the CH_4 selectivity stayed around 80%, and the CH_4 yield was about 41%.

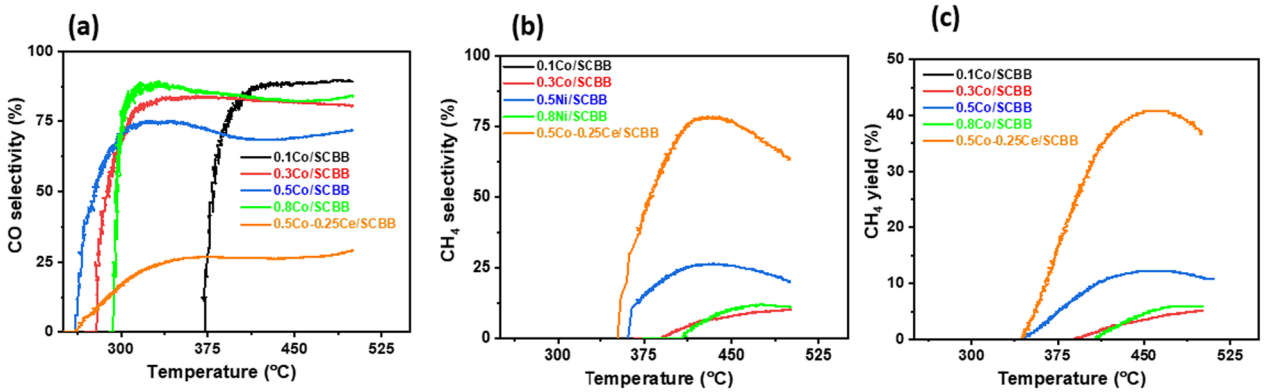

Fig. 8 **a** Methane selectivity, **b** Co selectivity, and methane yield (**c**) of all catalysts

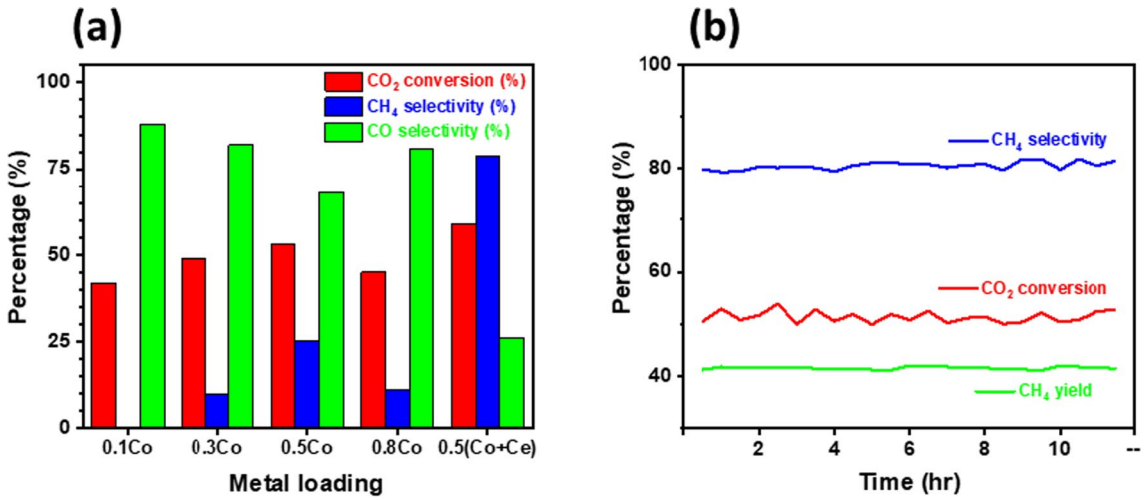

Fig. 9 **a** An evaluation of all catalysts at Conversion 500 °C and Selectivity 430 °C, and **b** stability test of 0.5 Co-0.25 Ce/SCBB at 430 °C

Only few reported bimetallic/biochar catalysts have been reported for the CO_2 methanation. However, all authors reported a significant improvement after the addition of Ce, as seen in Table 3. None of those reported studies investigated the Ce with Co supported on biochar as only that with Ni was investigated. Thus, this work was performed on the Co-Ce/biochar, and after comparing it with the reported monometallic Ni or bimetallic Ni-Ce/biochar catalysts, it is clear that the Co-Ce/SCBB catalyst can be considered as one of the active catalysts. For example, at atmospheric pressure, it offered 80% methane selectivity at 430 °C only, and Ni-Ce/BC catalyst (Renda et al. 2021) offered 88% but at higher operating temperature (450 °C) as seen in Table 3. On the other hand, Ni-Ce/BC catalyst (Stasi et al. 2021) showed a significant high catalytic performance with 95% methane selectivity at only 400 °C. However, the reaction was performed at the atmospheric pressure (10 bar) requiring higher cost.

4 Conclusion

The wet-impregnated sugarcane bagasse biochar (SCBB) by cobalt and cerium nanocatalysts worked effectively in the methanation reactions, attributed to the highly porous surface area composition offered by the sugar cane bagasse biochar. 0.5 Co/SCBB offered the best activity, as it showed the greatest carbon dioxide conversion and the best methane selectivity. However, 0.5 Co/SCBB could not achieve more than 27% methane selectivity at the optimal temperature, due to the existing agglomeration and the big particle size. On the other hand, the bimetallic 0.5 Co-0.25 Ce/SCBB showed higher catalytic performance than the monometallic 0.5 Co/SCBB, which is attributed to the effect of Ce that improved the metals dispersion on the support, and offered less particle size. The bimetallic catalyst 0.5 Co-0.25 Ce/SCBB achieved 51% carbon dioxide conversion, 80% methane selectivity, and 41% methane yield, at 430 °C, and stayed active and stable for more than 12 h. This study opens the way for utilizing Ce to enhance various metals that cannot offer

Table 3 A comparative table for the limited investigated bimetallic biochar-supported catalysts

Sample	Synthesis	Parameter	%CO_2 Conv	%Methane Sel	Reference
Ni/BC	Thermal decomposition	1 atm. at 450 °C	42	65	Renda et al. 2021
Ni + Ce/BC	Thermal decomposition	1 atm. at 450 °C	65	88	Renda et al. 2021
Ni/CDC	Thermal decomposition	1 atm. at 400 °C	52	67	Tarifa et al. 2021
Ni + Ce/CDC	Thermal decomposition	1 atm. at 400 °C	78	99.9	Tarifa et al. 2021
Ni/BC	Thermal decomposition	1 MPa. at 500 °C	45	45	Stasi et al. 2021
Ni + Ce/BC	Thermal decomposition	1 MPa. at 400 °C	65	95	Stasi et al. 2021
Co/SCBB	Thermal decomposition	1 atm. at 430 °C	40	26	Our work
Co + Ce/SCBB	Thermal decomposition	1 atm. at 430 °C	51	80	Our work

high catalytic activity in the carbon dioxide methanation alone.

Supplementary Information

The online version contains supplementary material available at https://doi.org/10.1007/s42773-025-00459-x.

Supplementary Material 1: Table SI1. Elemental surface composition of biochar samples as determined by XPS

Acknowledgements
The authors are indebted to the team of the Central Lab Unit (CLU) of Qatar University for their assistance with the required analyses. P. Decorse is acknowledged for XPS analysis at ITODYS Lab. We would like to extend our gratitude to the China Scholarship Council (CSC) for the provision of a PhD scholarship to Mengqi Tang (No, 202008310221).

Author contributions
Ahmed Gamal: investigation, writing original draft preparation. Mengqi Tang: investigation, formal analysis, data curation. Mohamed M. Chehimi: conceptualization, methodology, validation, writing—review and editing, data curation, resources. Ahmed M. Khalil: biomass collection and analysis. Kenneth I. Ozoemena: review and editing. Aboubakr M. Abdullah: conceptualization, review and editing, resources. Khouloud Jlassi: conceptualization, data curation, validation, review and editing, project administration, funding acquisition. All authors have read and approved the final manuscript.

Funding
Open Access funding provided by the Qatar National Library. This work was supported by the Qatar National Research Fund (QRDI, a member of the Qatar Foundation, through the National Priority Research Program Grant (ARG01-0530-230416).

Data availability
The datasets collected and analyzed during the current study are available from the corresponding author on reasonable request.

Declarations

Competing interests
All authors have no competing interests to disclose. The authors declare no conflict of interest that could have appeared to influence the presented work.

Author details
[1]Center for Advanced Materials, Qatar University, 2713 Doha, Qatar. [2]CNRS (UMR 7086), Université Paris Cité, ITODYS, 75013 Paris, France. [3]Photochemistry Department, National Research Centre, Dokki, Giza 12622, Egypt. [4]Molecular Sciences Institute, School of Chemistry, University of the Witwatersrand, Private Bag 3, PO Wits, Johannesburg 2050, South Africa.

Received: 15 October 2024 Revised: 22 February 2025 Accepted: 8 March 2025
Published online: 15 May 2025

References

Adeniyi AG et al (2023) One-step chemical activation for the production of engineered orange peel biochar. Emergent Mater 6:211–221
Ali S, Khader MM, Almarri MJ, Abdelmoneim AG (2020) Ni-based nano-catalysts for the dry reforming of methane. Catal Today 343:26–37
Ali S, Gamal A, Khader MM (2023) Development of highly active and coke-resilient Ni-based catalysts for low-temperature steam reformation of methane. Catal Commun. https://doi.org/10.1016/j.catcom.2023.106605
Bhakta AK et al (2023) Sweety, salty, sour, and romantic biochar-supported ZnO: highly active composite catalysts for environmental remediation. Emergent Mater. https://doi.org/10.1007/s42247-023-00599-5
Bhuvanendran N et al (2021) Spindle-shaped CeO2/biochar carbon with oxygen-vacancy as an effective and highly durable electrocatalyst for oxygen reduction reaction. Int J Hydrogen Energy 46:2128–2142
Chen H, Zhang Y, Li J, Zhang P, Liu N (2019) Preparation of pickling-reheating activated alfalfa biochar with high adsorption efficiency for p-nitrophenol: characterization, adsorption behavior, and mechanism. Environ Sci Pollut Res 26:15300–15313
Cho D-W et al (2018) Synthesis of cobalt-impregnated carbon composite derived from a renewable resource: characterization and catalytic performance evaluation. Sci Total Environ 612:103–110
Collet P et al (2017) Techno-economic and life cycle assessment of methane production via biogas upgrading and power to gas technology. Appl Energy 192:282–295
Di Stasi C et al (2021) Wheat-straw-derived activated biochar as a renewable support of Ni-CeO2 catalysts for CO2 methanation. Sustainability 13:8939
Eddaoudi M. (ACS Publications. 2005.
Frontera P, Macario A, Ferraro M, Antonucci P (2017) Supported catalysts for CO2 methanation: a review. Catalysts 7:59
Gac W et al (2020) Effects of support composition on the performance of nickel catalysts in CO2 methanation reaction. Catal Today 357:468–482
Gamal A et al (2024) CO2 methanation using sugarcane bagasse biochar/nickel sustainable catalysts. Mater Today Sustain 25:100627
Hu F et al (2019) Reduced graphene oxide supported Ni-Ce catalysts for CO2 methanation: the support and ceria promotion effects. J CO2 Util 34:676–687
Jiao G-J et al (2021) Nitrogen-doped lignin-derived biochar with enriched loading of CeO2 nanoparticles for highly efficient and rapid phosphate capture. Int J Biol Macromol 182:1484–1494
Khalil AM et al (2021) Copper/nickel-decorated olive pit biochar: one pot solid state synthesis for environmental remediation. Appl Sci 11:8513
Kumar A, Negi YS, Choudhary V, Bhardwaj NK (2014) Characterization of cellulose nanocrystals produced by acid-hydrolysis from sugarcane bagasse as agro-waste. J Mater Phys Chem 2:1–8
Lee WJ et al (2021) Recent trend in thermal catalytic low temperature CO2 methanation: a critical review. Catal Today 368:2–19
Leng L et al (2021) An overview on engineering the surface area and porosity of biochar. Sci Total Environ 763:144204
Pawelczyk E, Wysocka I, Gębicki J (2022) Pyrolysis combined with the dry reforming of waste plastics as a potential method for resource recovery—a review of process parameters and catalysts. Catalysts 12:362
Powell CJ (2012) Recommended Auger parameters for 42 elemental solids. J Electron Spectrosc Relat Phenom 185:1–3
Praline G, Koel BE, Hance R, Lee H-I, White J (1980) X-ray photoelectron study of the reaction of oxygen with cerium. J Electron Spectrosc Relat Phenom 21:17–30
Renda S, Di Stasi C, Manyà JJ, Palma V (2021) Biochar as support in catalytic CO2 methanation: enhancing effect of CeO2 addition. J CO2 Util 53:101740
Riani P et al (2023) Ni/Al2O3 catalysts for CO2 methanation: effect of silica and nickel loading. Int J Hydrogen Energy 48:24976–24995
Shen C, Liu M, He S, Zhao H, Liu C-J (2024) Advances in the studies of the supported ruthenium catalysts for CO2 methanation. Chin J Catal 63:1–15
Snoussi Y et al (2023) Green, zero-waste pathway to fabricate supported nanocatalysts and anti-kinetoplastid agents from sugarcane bagasse. Waste Manag 155:179–191
Song L, Wang H, Wang S, Qu Z (2023) Dual-site activation of H2 over Cu/ZnAl2O4 boosting CO2 hydrogenation to methanol. Appl Catal B 322:122137
Stangeland K, Li H, Yu Z (2020) CO 2 hydrogenation to methanol: the structure–activity relationships of different catalyst systems. Energy Ecol Environ 5:272–285
Tang M et al (2023) Unusual, hierarchically structured composite of sugarcane pulp bagasse biochar loaded with Cu/Ni bimetallic nanoparticles for dye removal. Environ Res 232:116232
Tang M et al (2024) Pyrolysis temperature effect on the efficacy of biochar/CuNi composite catalysts for emerging pollutant degradation. Surfaces Interfaces 50:104446
Tarifa P et al (2021) Highly active Ce-and Mg-promoted Ni catalysts supported on cellulose-derived carbon for low-temperature CO2 methanation. Energy Fuels 35:17212–17224

Thommes M et al (2015) Physisorption of gases, with special reference to the evaluation of surface area and pore size distribution (IUPAC Technical Report). Pure Appl Chem 87:1051–1069
Tripodi A, Conte F, Rossetti I (2020) Carbon dioxide methanation: design of a fully integrated plant. Energy Fuels 34:7242–7256
Valluri S, Claremboux V, Kawatra S (2022) Opportunities and challenges in CO2 utilization. J Environ Sci 113:322–344
Wang J, Mueller DN, Crumlin EJ (2024) Recommended strategies for quantifying oxygen vacancies with X-ray photoelectron spectroscopy. J Eur Ceramic Soc 44:116709
Wiśniewska M, Rejer K, Pietrzak R, Nowicki P (2022) Biochars and activated biocarbons prepared via conventional pyrolysis and chemical or physical activation of mugwort herb as potential adsorbents and renewable fuels. Molecules 27:8597
Yuan X et al (2013) Effects of cobalt precursor on pyrolyzed carbon-supported cobalt-polypyrrole as electrocatalyst toward oxygen reduction reaction. Nanoscale Res Lett 8:1–11
Zhang Z et al (2022) Advances in studies of structural effect of the supported Ni catalyst for CO2 hydrogenation: from nanoparticle to single atom catalyst. J Mater Chem A. https://doi.org/10.1039/D1TA09914K
Zhong L, Pham THM, Ko Y, Züttel A (2023) Graphene nanoplatelets promoted CoO-based catalyst for low temperature CO2 methanation reaction. Front Chem Eng 5:1160254
Zhong C et al (2024) Morphology effect of La2O2CO3 on CO2 methanation over Ni-based catalysts. Catal Lett. https://doi.org/10.1007/s10562-024-04738-3
Zhu QL, Xia W, Akita T, Zou R, Xu Q (2016) Metal-organic framework-derived honeycomb-like open porous nanostructures as precious-metal-free catalysts for highly efficient oxygen electroreduction. Adv Mater 28:6391–6398